ELSEVIER

Journal of Power Sources 77 (1999) 1–11

JOURNAL OF POWER SOURCES

Physical and electrochemical characterization of nanocrystalline $LiMn_2O_4$ prepared by a modified citrate route

J.-H. Choy *, D.-H. Kim, C.-W. Kwon, S.-J. Hwang, Y.-I. Kim

Department of Chemistry, Center for Molecular Catalysis, College of Natural Sciences, Seoul National University, Seoul 151-742, South Korea

Received 2 August 1998; accepted 3 September 1998

Abstract

Nanocrystalline $LiMn_2O_4$ spinel oxides have been synthesized successfully by using a modified citrate route with ethanol dehydration of a Li–Mn–citrate complex solution. The effects of sintering temperature and atmosphere on the physicochemical properties of the $LiMn_2O_4$ powders have been carefully examined by means of X-ray diffraction, electron microscopy, BET measurement, and X-ray absorption spectroscopy. It becomes clear that an oxidative atmosphere induces a partial agglomeration of particles at high temperature, but gives rise to an effective decomposition of the citrate precursors at low temperature. It is also found that a lowering of the sintering temperature enhances the average oxidation state of manganese with an increase in surface defects. The electrochemical property of the present $LiMn_2O_4$ nanocrystals has also been measured to compare with that of lithium manganate prepared by a solid-state reaction, which confirms the effectiveness of the present modified citrate route. The evolution of geometrical and electronic structures during the charging process has also been investigated with X-ray absorption spectroscopy, and reveals shortening of the (Mn–O) bond distances induced by lithium de-intercalation.

Keywords: $LiMn_2O_4$ nanocrystal; Modified citrate route; Oxidative atmosphere; Sintering temperature; Charging process

1. Introduction

By virtue of its low cost, low toxicity and high electrical potential, $LiMn_2O_4$ spinel oxide is a good candidate for the positive electrode (cathode) in rechargeable lithium batteries [1–4]. This material can be used not only for the 4-V region corresponding to lithium de-intercalation, but also for the 3-V region corresponding to lithium intercalation, as represented in the following equation [5,6];

$$Mn_2^{4+}O_4 \overset{4V}{\leftrightarrow} LiMn^{3+}Mn^{4+}O_4 \overset{3V}{\leftrightarrow} Li_2Mn_2^{3+}O_4.$$

It is well-known that the discharge process (right-hand reaction) results in a tetragonally distorted $Li_2Mn_2O_4$ induced by the Jahn–Teller effect of octahedral Mn^{3+} (high spin d^4) [6,7]. In this context, the observed considerable capacity fading for this region might be related to this structural phase transition with significant unit-cell expansion (about 4%) [8,9]. By contrast, the charging process (left-hand reaction) exhibits a smaller capacity loss with respect to the right-hand reaction. But, for this region, there are some factors such as particle size and surface morphology, which have an important influence upon the long-term cycling characteristics [10–13]. It is difficult, however, to control such factors precisely using a conventional solid-state reaction which requires a high reaction temperature, long and repeated heat treatments, and a post-calcination step that lead to the agglomeration of particles. Such difficulties are expected to be solved by using solution techniques where all the components can be homogeneously distributed to an almost atomic scale, thus allowing a reduction in the heating temperature and the sintering time. For this reason, various solution methods have been investigated to prepare $LiMn_2O_4$ with a better electrochemical performance. For example, Barboux et al. [8] have obtained the spinel phase at a low temperature of 300°C by using a precipitation method with LiOH and manganous nitrate or acetates. This method has been modified both by replacing LiOH with Li_2CO_3 and by introducing carbon into the solution process [14]. Other attempts

* Corresponding author. Tel.: +82-2-880-6658; Fax: +82-2-872-9864; E-mail: jhchoy@plaza.snu.ac.kr

0378-7753/99/$19.00
PII: S0378-7753(98)00157-8

have been made to synthesize the $LiMn_2O_4$ spinel with polymeric and carboxylic precursors, such as PEG (polyethylene glycol) [15], fumaric [16] and tartaric acids [17]. In addition to these methods, the citrate route is expected to be quite useful in preparing such multicomponent oxides with a high chemical homogeneity and a small particle size [18–23]. Nevertheless, this method has not been used widely for the synthesis of $LiMn_2O_4$ [22,23], which might be due to the fall in pH of the complex solution during water evaporation that gives rise to recrystallization of the Li-deficient lithium–manganese–citrate complex. In practice, the heat treatment of such a complex causes the formation of a mixed phase of $LiMn_2O_4$ and MnO or Mn_2O_3. To solve this problem, we have adopted a modified citrate route of ethanol dehydration [20,21], which is based on the low solubility of citrate salts in ethanol with respect to water. A dropwise addition of aqueous metal citrate solution into ethanol causes rapid precipitation to provide a very fine and homogeneous citrate precursor.

In this paper, we report the successful synthesis of $LiMn_2O_4$ nanoparticles by a modified citrate route where ethanol is used as a dehydration agent. The effect of the synthesis conditions on the physicochemical properties of the products has been examined systematically by using powder X-ray diffraction (XRD), scanning electron microscopy (SEM), transmission electron microscopy (TEM), BET surface-area measurements, X-ray absorption spectroscopy (XAS), and electrochemical measurements. In addition, X-ray absorption near edge structure (XANES) and extended X-ray absorption fine structure (EXAFS) analyses have been carried out on the $LiMn_2O_4$ spinel before and after lithium de-intercalation, in order to elucidate any variations in the crystal and the electronic structures that may be induced by the charging process.

2. Experimental

The citrate precursor was obtained by an ethanol dehydration method, as described below [20,21]. At first, $Mn(NO_3)_2 \cdot 4H_2O$ (Aldrich, $> 98\%$) was dissolved in a minimal amount of deionized water to give a saturated solution (about 60 wt.%). The deionized water was decarbonated prior to use. To this solution, Li_2CO_3 (Aldrich, 99%) was added slowly with mild stirring. A saturated aqueous solution of citric acid (about 40% in weight) was then added at a molar ratio of Li:Mn:citric acid = 1.2:2:3.2. The pH of the mixed solution was maintained at 6.5 to 7.0 by adding NH_4OH solution heated to 80°C for 30 min, not only to complete the reaction but also to remove excess ammonia. The resulting pale-pink solution was then added drop by drop into absolute ethanol with vigorous stirring to give a rapid precipitation of metal citrate. The precipitate was filtered, washed with ethanol, and finally dried at 100°C in air. After drying, the resulting powder was heated at 250°C for 6 h in order to achieve an esterification of the citrate precursors. The obtained black solids were sintered at different temperatures, viz., 300, 400, 500, 600, and 700°C, in air or oxygen. During the heating and cooling, the rate of temperature variation was fixed at 1°C per minute. For clarity, the final products are denoted as follows: samples prepared at n00°C ($n = 3$, 4, 5, 6, and 7) in air and oxygen are represented as SPNnA and SPNnO, respectively. The detailed reaction conditions for each sample are discussed in Section 3. In order to check out the usefulness of the present citrate route, $LiMn_2O_4$ was also prepared by a solid-state reaction in which Li_2CO_3 (10% excess) and MnO_2 were thoroughly mixed, calcined at 650°C for 12 h, and then sintered twice at 800°C for 24 h with intermediate grindings.

The thermal behaviour of lithium–manganese–citrate precursor was monitored by thermogravimetry (TG) and differential thermal analysis (DTA) by means of a Rigaku TAS-100 thermal analyzer. The samples were heated at a rate of 2°C per minute from 20 to 700°C in air and oxygen atmospheres. The crystal structure was examined with a powder X-ray diffractometer (Phillips PW1830) which was equipped with Ni-filtered Cu K_α radiation ($\lambda = 1.5418$ Å). The morphology and particle size of the samples were probed both by SEM using a JEOL JSM-840 Microscope

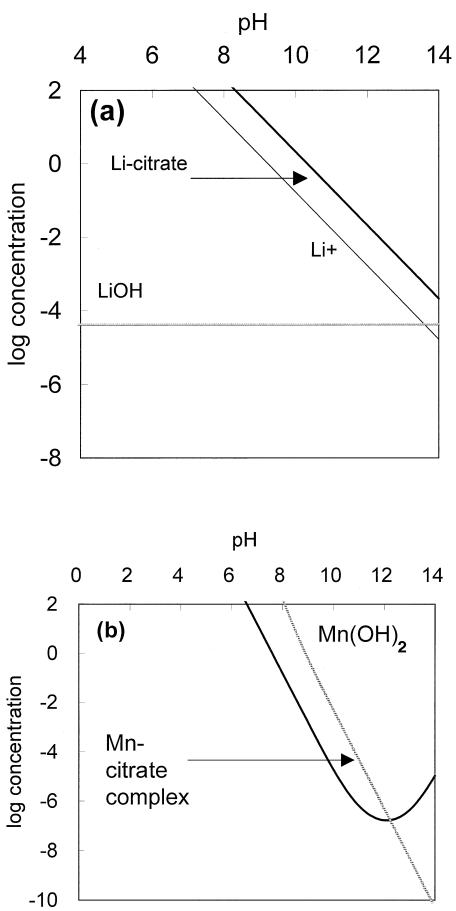

Fig. 1. Solubility isotherms for (a) Li_2CO_3–citric acid–H_2O and (b) $Mn(OH)_2$–citric acid–H_2O systems as a function of pH.

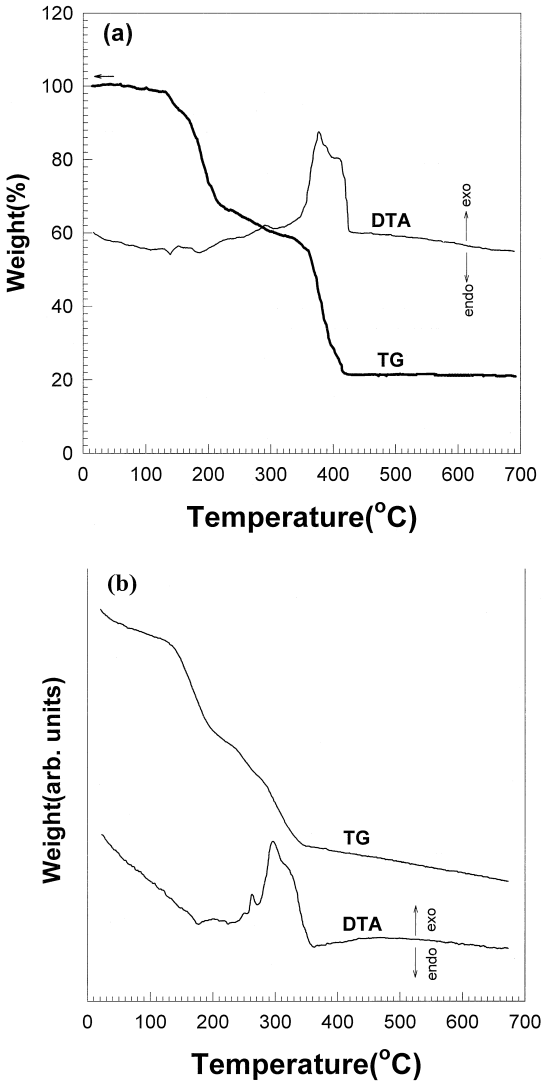

Fig. 2. TG-DTA curves for Li–Mn-citrate precursor in (a) air and (b) oxygen.

with 20 k magnification, and by TEM using a JEM-2000 EX II microscope with 100 and 200 k magnifications. The BET specific surface area was calculated from the N_2 adsorption isotherm measured at 77 K.

Electrochemical measurements were performed on a cell of Li/1M $LiPF_6$ in EC:DMC (50:50 v/v)/$LiMn_2O_4$, which was assembled in a dry box with an argon inert atmosphere. The composite cathodes were prepared by intimately mixing the active material (88 wt.%) with 10 wt.% acetylene black and 2 wt.% PTFE (polytetrafluoroethylene). All experiments were performed in a galvanostatic mode at C/10 (at a constant current that can reach $x = 1$ in $Li_xMn_2O_4$ for 10 h) with an Arbin BT 2043 multichannel galvanostat/potentiostat in the voltage range of 3.5 to 4.5 V.

X-ray absorption experiments were carried out on the beam line 3C1 of Pohang Light Source (PLS), operated at 2.0 GeV with a ring current of 80 to 100 mA. The samples were ground finely and spread uniformly onto an adhesive tape by nujol. The tape was folded into a few layers to obtain an appropriate absorption jump, i.e., sufficient to be free from thickness and pinhole effects. All the data were collected in a transmission mode using a Si (311) double crystal monochromator and a N_2-filled ionization detector with a spacing of ~ 0.4 and ~ 1.5 eV for the XANES and EXAFS regions, respectively. For each measurement, the energy calibration was carried out by simultaneously recording the spectrum of manganese metal. Data analysis of the experimental spectra was performed with the computer program, UWXAFS [24], which employed curved wave theory using the scattering parameters obtained by ab initio FEFF6 code [25].

3. Results and discussion

The solubility isotherms for the Li_2CO_3–citric acid–H_2O system are shown in Fig. 1(a) as a function of $\log[Li^+]$ and pH. The considered chemical species and their thermodynamic equilibrium constants are summarized in Table 1. In this system, the possible precipitates are taken to be LiOH(s) and Li_2CO_3(s). The LiOH(s) is so highly soluble in an aqueous solution that it can be precipitated only in a fairly basic region ($pH > 13$). Thus, the Li_2CO_3 is reasonably regarded as the most stable solid phase in an atmospheric environment ($P_{CO_2} = 10^{-3.5}$ atm). According to the solubility isotherm, the precipitation of lithium carbonate is predicted to start at $pH \cong 10$ for $[Li^+] = 0.1$ M. The solubility of lithium carbonate is ex-

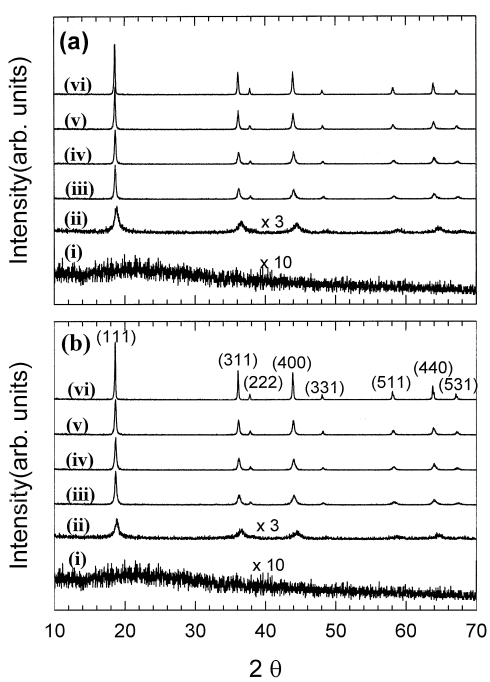

Fig. 3. Powder XRD patterns of $LiMn_2O_4$ prepared in (a) air and (b) oxygen at: (i) 250, (ii) 300, (iii) 400, (iv) 500, (v) 600, and (vi) 700°C.

pected to be increased by the presence of citric acid, since it gives rise to the formation of soluble Li–citrate complexes such as $LiC_6H_5O_7^{2-}$. In Fig. 1(a), the total concentration of the soluble Li–citrate complexes in equilibrium with a solid lithium carbonate is marked as a thick solid line, and reveals that lithium carbonate is not precipitated below pH = 12 in the presence of citric acid. The solubility isotherms of the $Mn(OH)_2$–citric acid–H_2O system are illustrated in Fig. 1(b), together with the distribution of various chemical species. In this aqueous solution, Mn^{2+} is hydrolyzed and precipitated as $Mn(OH)_2$(s). According to the solubility isotherm of $Mn(OH)_2$(s) (thin solid line), the precipitation of manganese hydroxide begins at around pH = 6, in the absence of citric acid. Since the citric acid takes part in the complex formation with manganese, the solubility of $Mn(OH)_2$(s) is largely increased by adding citric acid, which causes the hydroxide to precipitate at pH = 8. In other words, pure and stable Mn–citrate complexes can be obtained at $pH \leq 8$. On the other hand, taking into account the dissociation of citric acid, it is desirable to work at $pH > pK_3$ (6.4) for ensuring the complete dissociation of citric acid. Moreover, the solution pH should be maintained at $pH < 10$, in order to obtain pure and stable citrate complexes of lithium and manganese. In this regard, the optimum pH for the synthesis of pure and stable metal citrate complexes is determined to be 6.5 to 7.5, where the formation of impurity phases such as carbonates and hydroxides is effectively suppressed.

The thermal behaviour of the citrate precursors in air and oxygen is compared in Fig. 2. For the TG curve recorded in air, four main weight-loss domains are observed in the temperature ranges of 25–120, 120–170, 170–250, and 250–430°C. While the first domain is attributed to the dehydration of surface water, the next two domains which correspond to the endothermic peaks at 140 and 190°C in the DTA curve are assigned to the

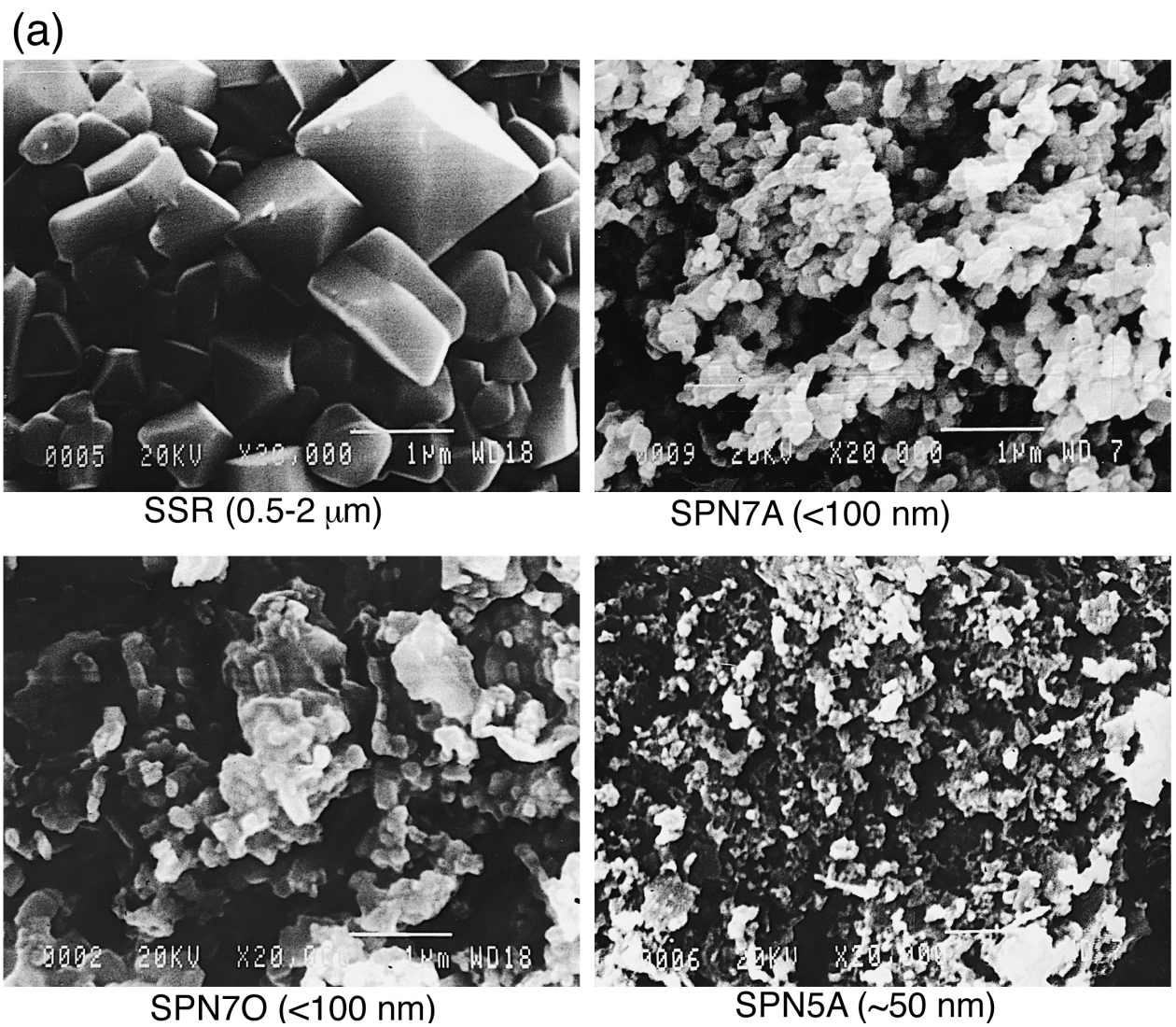

Fig. 4. (a) Scanning electron micrographs for $LiMn_2O_4$ particles, SSR, SPN7A, SPN7O, and SPN5A. (b) Transmission electron micrographs for SPN7A (left top), SPN7O (right top), SPN5A (right bottom), and SPN5O (left bottom).

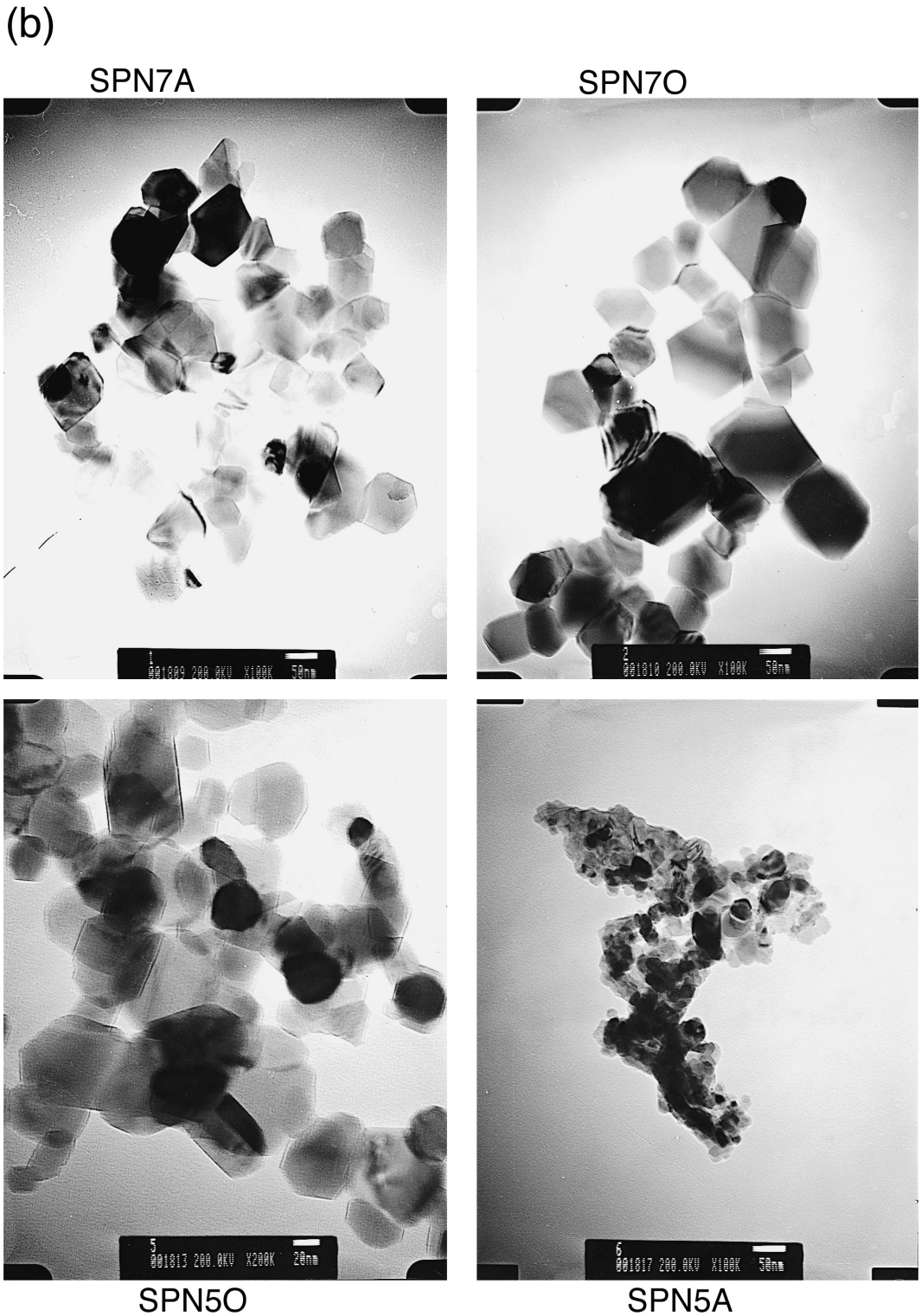

Fig. 4 (continued).

evolution of NH_3 and the dehydration of citrate ($C_6H_5O_7^{3-}$) to itaconate ($C_5H_4O_4^{2-}$) through aconitate ($C_6H_3O_6^{3-}$), respectively [18,21]. Assuming that all the citric acids participate in the complex formation, the chemical formula of the citrate precursor is estimated to be $(NH_4)_4LiMn_2(C_6H_5O_7)_3$. Based upon this formula, the weight loss in the second domain is attributed to the reaction $(NH_4)_4LiMn_2(C_6H_5O_7)_3 \rightarrow H_4LiMn_2(C_6H_5O_7)_3 + 4NH_3$ of which the observed weight loss (8.5%) is in good agreement with the theoretical

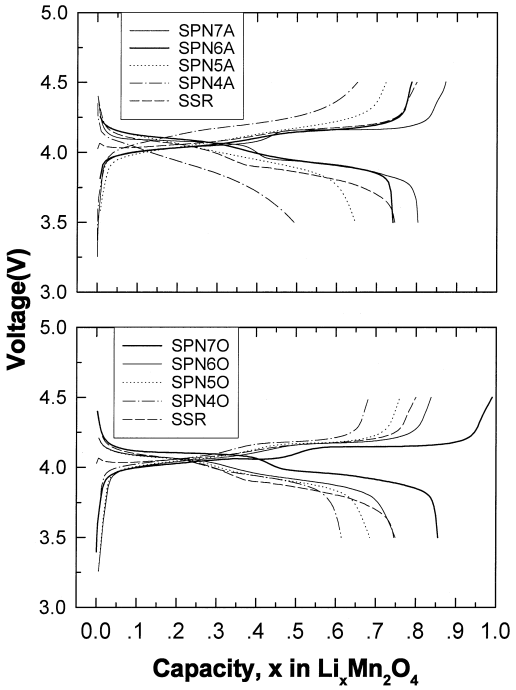

Fig. 5. Voltage profiles on first cycle of lithium intercalation/de-intercalation of $LiMn_2O_4$ samples in 4-V domain.

value (9.0%). The third domain is ascribed to the reaction $H_4LiMn_2(C_6H_5O_7)_3 \rightarrow HLiMn_2(C_5H_4O_4)_3 + 3CO_2 + 3H_2O$, which is confirmed by a good agreement between the observed weight loss (29.0%) and the calculated value (28.0%). A fourth drastic weight loss is detected in the temperature range 300 to 430°C, and is ascribed to the combustion of residual organics. In addition to these weight losses, a slight increase in sample weight

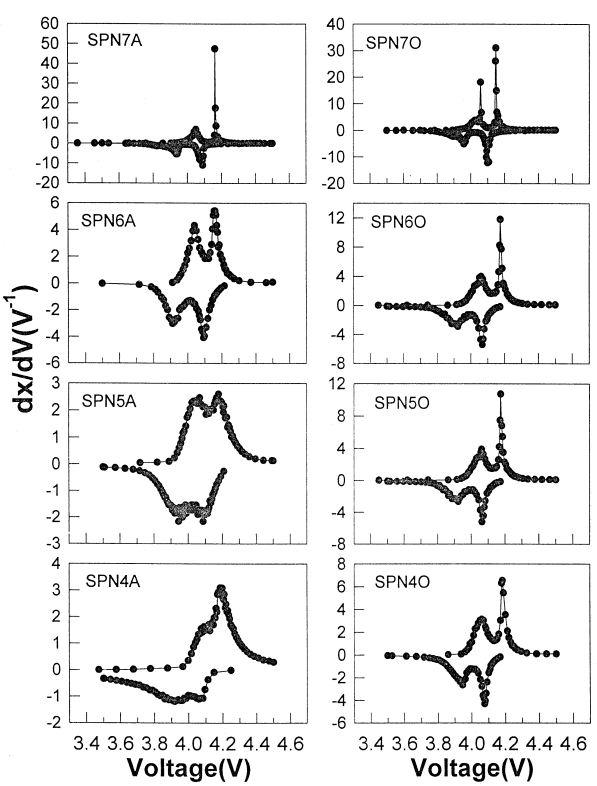

Fig. 6. dx/dV plots of $Li_xMn_2O_4$ samples in 4-V domain.

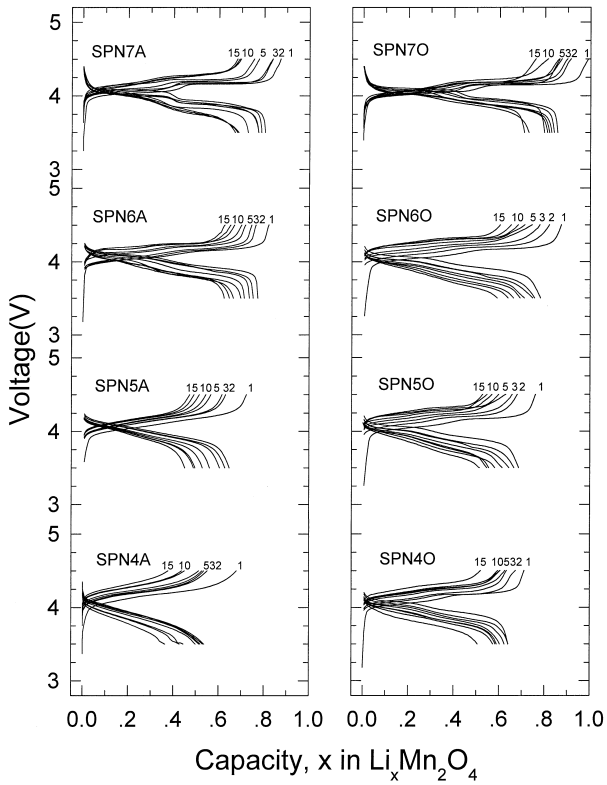

Fig. 7. Evolution of electrochemical characteristics from 1st to 15th cycle for $LiMn_2O_4$ samples in 4-V domain.

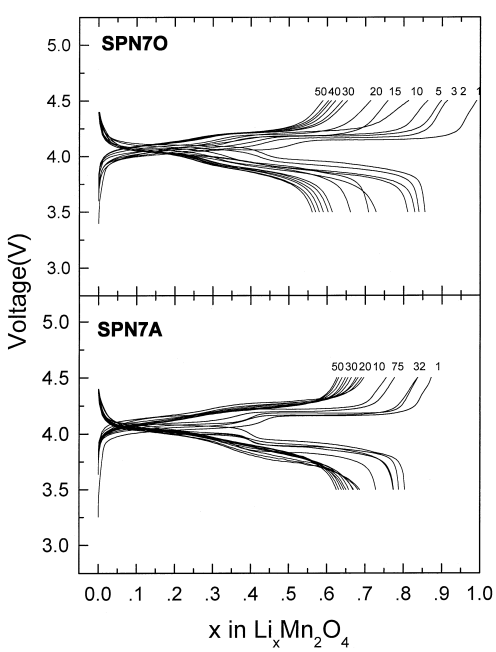

Fig. 8. Long-term cycle characteristics of samples SPN7A and SPN7O in 4-V domain.

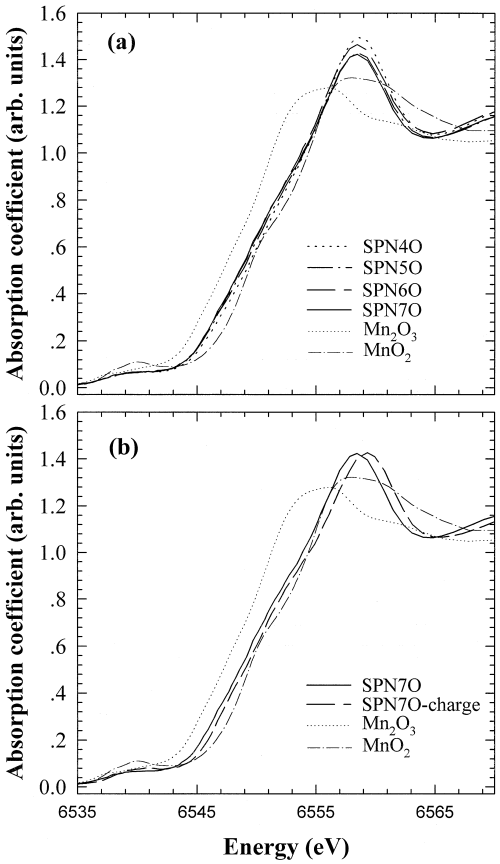

Fig. 9. Mn K-edge XANES spectra for (a) $LiMn_2O_4$ spinels, SPN4O, SPN5O, SPN6O, and SPN7O, and (b) SPN7O before and after Li de-intercalation, in comparison with those for reference samples of MnO_2 and Mn_2O_3.

(not more than 1%) is observed over the temperature range 420 to 500°C and indicates a slight uptake of oxygen by spinel lattice. From the present TG curve, the total weight loss is determined to be 77.4%, which coincides well with the calculated value of 76.1% for $(NH_4)_4LiMn_2(C_6H_5O_7)_3$. As shown in Fig. 2(b), an oxygen atmosphere shifts the two exothermic peaks towards lower temperatures and decreases the decomposition temperature of the organic residues. This shows that oxygen can accelerate the combustion of citrate frameworks in the precursor. From the above experimental findings, it is expected that organic-free $LiMn_2O_4$ spinel particles can be obtained at a low temperature of 400°C, and that the heating time has to be extended to prepare spinel particles in an ambient atmosphere as opposed to an oxygen one.

Powder XRD patterns for $LiMn_2O_4$ prepared by heating the citrate precursor at various temperatures in air and oxygen are shown in Fig. 3. For the samples obtained at 300°C, a broad base-line is observed together with sharper peaks which correspond to the spinel phase, even after an extended heat treatment for more than 72 h. Such a broad base-line can be eliminated by heating above 400°C. As the heat-treatment temperature increases, the XRD peak is found to be enhanced with a decrease of full-width-at-half-maximum (FWHM). This suggests the growth of $LiMn_2O_4$ crystallites. All the XRD patterns are well indexed with a cubic symmetry and the cell parameters obtained from the least-square fitting analysis are listed in Table 2. It is certain that the cell parameters gradually increase with increasing heating temperature, and that the samples prepared in air have slightly larger unit cells than those obtained in oxygen.

In order to probe the relationship between sintering temperature and crystal growth, the particle size of $LiMn_2O_4$ has been estimated by various methods, namely, XRD, SEM, TEM, and BET surface-area measurement. At first, the crystallite size (t) is estimated from the XRD pattern with the aid of Scherrer's formula, $t = 0.9\ \lambda/(B\cos\theta)$, where λ is the X-ray wavelength ($\lambda = 1.5418$ Å) and B is the FWHM of the XRD peak in radians [29]. On the other hand, based on an assumption that the shape of the particle is an ideal cube, the particle size is calculated from BET measurements by using the relationship $A = 6/(\rho l)$, where A is the specific surface area, ρ is the density, and l is the particle size [30]. The results are given

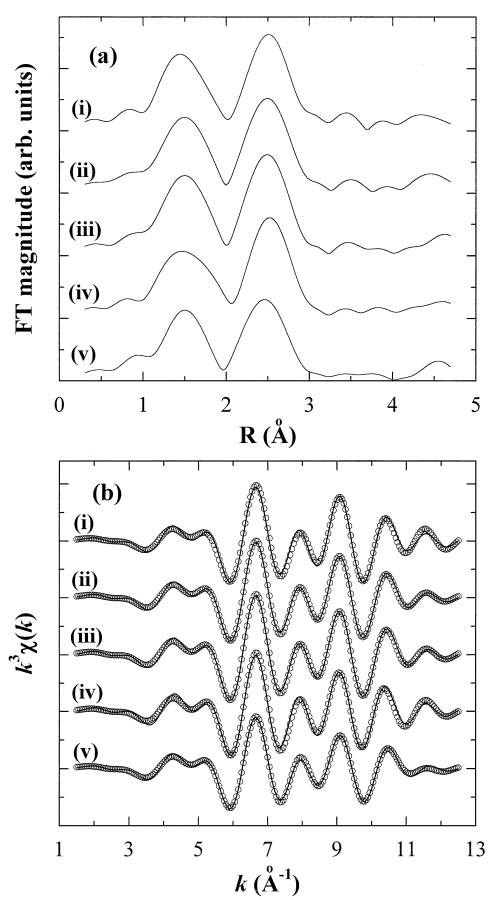

Fig. 10. (a) Fourier transformed Mn K-edge EXAFS spectra and (b) their inverse Fourier transforms for $LiMn_2O_4$ spinels: (i) SPN4O, (ii) SPN5O, (iii) SPN6O, (iv) SPN7O, and (v) charged SPN7O.

Table 1
Equilibria and the constants used in this calculation

Equilibrium reaction	Symbol	log (constant)	Ref.
$Li_2CO_3(s) \leftrightarrow 2Li^+ + CO_3^{2-}$	K_{sp}	−3.1	[26]
$Li^+ + H_2O \leftrightarrow LiOH^0(aq) + H^+$	β_1*	−13.6	[27]
$Li^+ + C_6H_5O_7^{3-} \leftrightarrow LiC_6H_5O_7^{2-}$	β_1	0.8	[28]
$Mn(OH)_2(s) \leftrightarrow Mn^{2+} + 2OH^-$	K_{sp}	−12.8	[26]
$Mn^{2+} + H_2O \leftrightarrow MnOH^+ + H^+$	β_1*	−10.59	[27]
$Mn^{2+} + 2H_2O \leftrightarrow Mn(OH)_2^0(aq) + 2H^+$	β_2*	−22.2	[27]
$Mn^{2+} + 3H_2O \leftrightarrow Mn(OH)_3^- + 3H^+$	β_3*	−34.8	[27]
$Mn^{2+} + 4H_2O \leftrightarrow Mn(OH)_4^{2-} + 4H^+$	β_4*	−48.3	[27]
$Mn^{2+} + C_6H_5O_7^{3-} \leftrightarrow MnC_6H_5O_7^-$	β_1	4.2	[28]
$Mn^{2+} + C_6H_6O_7^{2-} \leftrightarrow MnC_6H_6O_7^0(aq)$	β_2	2.2	[28]
$C_6H_8O_7 \leftrightarrow C_6H_7O_7^- + H^+$	K_1	−3.1	[28]
$C_6H_7O_7^- \leftrightarrow C_6H_6O_7^{2-} + H^+$	K_2	−4.8	[28]
$C_6H_6O_7^{2-} \leftrightarrow C_6H_5O_7^{3-} + H^+$	K_3	−6.4	[28]

in Table 3, and are compared with the crystal sizes determined from electron microscopy. The data reveal a decreasing trend in crystallite size on lowering the heating temperature.

The dependence of particle size and morphology on the synthesis conditions has been examined by using SEM and TEM microscopy, as shown in Fig. 4. Scanning electron micrographs reveal that SPN7O and SPN7A particles exhibit uniform crystal shape and good crystallinity with an average size of ~100 nm, while SPN5A particles have an irregular and indistinct shape as well as a smaller size than those of high-temperature samples. Although the sintering atmosphere has little influence on the size of both SPN7A and SPN7O particles, the agglomeration of grains is more significant for SPN7O than for SPN7A particles. This is also confirmed from TEM images which show a broad distribution of particle size for the SPN7O sample. In the case of SPN5A with a quite small particle size of 20 to 80 nm, overall TEM images exhibit a substantial particle aggregation and a poorly developed crystal shape, as observed for SPN7O. The origin of particle aggregation for the low-temperature samples is thought to be different to that for SPN7O. That is, while the agglomeration at high temperature originates from a high degree of crystallization, the aggregation at low temperature is closely related to the presence of amorphous impurity phases such as Mn_xO_y, residual organics, and an incompletely converted non-stoichiometric spinel phase. In fact, it has been reported [31,32] that, at low temperatures below 500°C, the stoichiometric spinel is so unstable in air that it can be easily decomposed to lithium-rich spinel analogues which lead to the formation of relatively small particle sizes with ill-developed microcrystallites. In this respect, it is expected that the aggregates in low-temperature samples are less rigid than those in high-temperature ones, and that they possess many micro-pores inside the grains, which is supported by the present BET data. As shown in Table 3, the surface area increases as the heating temperature decreases. The high surface area of the SPN5A and SPN5O samples is related not only to their small particle sizes but also to the existence of micropores in the inter-spaces of the loosely agglomerated particles. A sudden decrease in surface area is observed for the SPN4A sample which has the smallest particle size. This is due to the fact that organic species still remain in the grain boundaries as amorphous phases which may disturb a smooth gas adsorption.

The capacity-potential profiles of the first cycle of the electrochemical lithium intercalation/de-intercalation are depicted in Fig. 5 for the potential range 3.5 to 4.5 V (vs. Li/Li^+), and the corresponding numerical data are summarized in Table 4. The samples synthesized by the present citrate route are found to have a superior initial lithium intercalation capacity (Q_1) to that of the sample prepared by solid-state reaction at 800°C. This underlines the usefulness of the present citrate route. For the samples made from the citrate precursors, the initial capacity is found to increase with elevation of the sintering temperature. This can be interpreted as a result of prominent cationic mixing and surface defects in low-temperature samples that hinder an effective de-intercalation of lithium. As shown in Fig. 5, all the present samples except SPN5A and SPN4A, exhibit two distinct plateau around 4 V in both charge and discharge curves, as observed for the spinel $LiMn_2O_4$ prepared by other methods. The first plateau at 4.05 V is associated with the reversible reaction $LiMn_2O_4 \rightarrow Li_{0.5}Mn_2O_4 + 0.5Li^+$, while the second one at 4.15 V (plateau B) is attributed to the reaction of $Li_{0.5}Mn_2O_4 \rightarrow Mn_2O_4 + 0.5Li^+$. The absence of these plateau for samples SPN5A and SPN4A is due to their defective morphology and absence of structural ordering during lithium de-intercalation. In contrast to the SPN*n*A series, the voltage profiles of SPN*n*O series show clearly both the existence of a flat potential region, even for the sample obtained at low temperature, and an increase in the plateau voltage with lowering of the heat-treatment temperature. This suggests that oxygen annealing at a low temperature facilitates the formation of the spinel phase by removing the organic species.

Table 2
Cell parameters obtained from XRD patterns

Sample		Heating condition	Lattice parameter (Å)
	SPN7A	700°C, 6 h	8.244_2
In air	SPN6A	600°C, 12 h	8.229_3
	SPN5A	500°C, 24 h	8.223_2
	SPN4A	400°C, 48 h	8.208_4
	SPN7O	700°C, 6 h	8.238_3
In oxygen	SPN6O	600°C, 12 h	8.226_4
	SPN5O	500°C, 24 h	8.219_3
	SPN4O	400°C, 48 h	8.207_3
SSR[a]		800°C, 48 h, in air	8.233_2

[a]SSR represents the sample prepared by the conventional solid-state reaction.

Table 3
Particle size estimated by electron microscopy, Scherrer's equation, and BET surface area

Sample		Electron microscopy (nm)	Scherrer's equation (nm)	BET surface area
	SPN7A	70 ~ 120	95	174 nm (8 m^2/g)
In air	SPN6A	50 ~ 100	60	87 nm (16 m^2/g)
	SPN5A	30 ~ 60	55	63 nm (22 m^2/g)
	SPN4A	20 ~ 60	45	116 nm (12 m^2/g)
	SPN7O	80 ~ 150	93	199 nm (7 m^2/g)
In oxygen	SPN6O	60 ~ 100	59	93 nm (15 m^2/g)
	SPN5O	30 ~ 80	55	70 nm (20 m^2/g)
	SPN4O	50 ~ 80	47	54 nm (26 m^2/g)
SSR[a]		500 ~ 2000	–	1395 nm (1 m^2/g)

[a]SSR represents the sample prepared by the conventional solid state reaction.

In order to obtain detailed information on the structural ordering upon lithium intercalation, the exact positions of the above two plateau are determined by plotting the *differential* capacity (dx/dV) as a function of voltage [32]. The dx/dV plots for the first lithium intercalation/de-intercalation cycle are shown in Fig. 6. In contrast to the other samples, only sample SPN4A fails to exhibit well-defined features, which makes it difficult to determine exactly the peak positions. Since the two peaks and the minimum between them are attributed to the sequence disorder–order–disorder which occurs on lithium de-intercalation, the ambiguous features of SPN4A indicate a structural disorder in the crystal lattice due to the low sintering temperature and the compositional impurity. Generally, the gap between the cathodic and the anodic peak positions for plateau A and B becomes larger as the temperature of heat treatment is lowered, irrespective of the preparative atmosphere. While the smallest peak voltage difference shown by sample SPN7O is strongly related to its highest first charge/discharge capacity, the largest peak gaps for samples SPN4A, SPN4O, and SPN5A are caused mainly by their defective crystal structures, which are observed by SEM and TEM.

From the long-term cycling characteristics given in Fig. 7 and Table 4, it becomes clear that both samples SPN7A and SPN6A exhibit the largest first cycle coulombic efficiency ($CE = Q_{discharge}/Q_{charge}$) among all the present samples. For these two samples, the coulomb efficiency on the nth cycle ($Q_{n,discharge}/Q_{n,charge}$) is found to be close to unity, which is comparable with the values for samples SPN7O and SPN6O. By contrast, the samples SPN5A and SPN4A prepared at low temperature show a smaller initial coulombic efficiency than SPN5O and SPN4O. Such dependence of cycleability on sintering atmosphere is attributed to a remarkable agglomeration of oxygen-annealed samples at high temperature and to a poor microstructure of air-annealed samples at low temperature.

Table 4
Variation of charge/discharge capacity and Coulomb efficiency during repeated cycles

Sample	Capacity (x in $Li_xMn_2O_4$)			Coulomb efficiency	
	1st charge	1st discharge	15th discharge	1st cycle	15th cycle
SPN7A	0.87	0.80	0.67	0.92	0.99
SPN6A	0.79	0.74	0.60	0.94	1.00
SPN5A	0.72	0.65	0.45	0.89	0.94
SPN4A	0.65	0.50	0.35	0.76	0.93
SPN7O	0.99	0.87	0.71	0.86	0.93
SPN6O	0.84	0.75	0.57	0.89	0.98
SPN5O	0.76	0.69	0.51	0.90	0.97
SPN4O	0.68	0.61	0.43	0.89	0.93

The variation of discharge capacity during extended cycling has been investigated for both samples SPN7A and SPN7O (Fig. 8). Even though sample SPN7O has a higher initial capacity than SPN7A, the rate of capacity reduction is more rapid for the former than for the latter. For the air-annealed sample, in particular, the discharge capacity of ≥ 90 mAh/g (0.61 mole of lithium) remains virtually unchanged after 50 cycles. Such difference in capacity fading between oxygen- and air-annealed samples might be related to their uniformity of particle shape and size, as confirmed by SEM and TEM. That is, a cathode consisting of homogeneous particles is expected to have a regular network which can maintain a uniform intercalation reversibility of each particle through repeated cycles. On the contrary, the heterogeneous and partially agglomerated particles in the oxygen-annealed sample may have different reactivity depending upon the grain size. This disparity among particles with various sizes is considered to increase as the cycling proceeds, and results in a decrease in the reversibility of the electrode.

In order to examine the effect of sintering temperature on the electronic and geometric structures of $LiMn_2O_4$ powders, systematic XANES/EXAFS analyses have been performed for the SPNnO series ($n = 4$, 5, 6, and 7). The Mn K-edge XANES spectra for the $LiMn_2O_4$ spinels are shown in Fig. 9(a), together with those for reference samples of Mn_2O_3 and MnO_2. The edge energies of lithium manganates are found to be lower than that of the Mn^{4+} reference, but higher than that of Mn^{3+} one. This indicates a mixed oxidation state of manganese (Mn^{3+}/Mn^{4+}) in these compounds. It is also observed that the edge energy is slightly increased as the sintering

temperature is decreased from 700 to 400°C, suggesting an increase in the Mn oxidation state with lowering of the sintering temperature. The effect of synthetic temperature on the crystal structure of $LiMn_2O_4$ spinel oxide has also been investigated by using Mn K-edge EXAFS analysis. The k^3 weighted EXAFS spectra for the $LiMn_2O_4$ spinel oxides, SPN*n*O ($n = 4$, 5, 6 and 7), were Fourier transformed (FT) with a k range of 3.8 to 11.8 $Å^{-1}$, as shown in Fig. 10(a). It is clearly detected from the FT diagram that both lithium manganates exhibit two intense peaks at ~ 1.6 and ~ 2.6 Å, which are attributed to the (Mn–O) and (Mn–Mn) bonding pairs, respectively. These FT peaks are isolated by an inverse Fourier transform to k space. The resulting $k^3\chi(k)$ Fourier filtered EXAFS oscillations are represented in Fig. 10(b), and the curve-fitting analyses have been carried out in order to determine the structural parameters such as coordination number (CN), bond distance (R), and Debye–Waller factor (σ^2). The best fitting results are compared with the experimental spectra in Fig. 10(b), and the fitted structural parameters are listed in Table 5. As shown in Fig. 10(b), the experimental spectra are in good agreement with the calculated spectra based on the spinel structure, demonstrating that the single-phase $LiMn_2O_4$ spinel oxides are obtained over the present range of sintering temperature. From the fitting results, the (Mn–O) and (Mn–Mn) bond distances are found to become shorter as the heat-treatment temperature is lowered. This confirms an enhancement of Mn oxidation state in the low-temperature phase. A conclusion is in a good agreement with the XRD results which show a decrease in the lattice parameter upon lowering of the sintering temperature. In addition to the variation in bond distances, the coordination numbers around manganese are found to be diminished with decrease in the heat-treatment temperature, which confirms a decrease of particle size for low-temperature phase, leading to unsaturated coordination around manganese near the surface.

The effect of lithium de-intercalation on the electronic and crystal structures of lithium manganate is also examined by performing XANES/EXAFS analyses. Fig. 9(b) shows the Mn K-edge XANES spectra for sample SPN7O before and after the charging process. The position of the edge jump of sample SPN7O is found to shift towards the high energy side upon lithium de-intercalation. In fact, the charged sample SPN7O exhibits nearly the same edge energy as the reference MnO_2, which indicates that the average oxidation state of manganese is increased by the charging process resulting in λ-MnO_2 with tetravalent manganese ion. The evolution of the local structure around manganese upon lithium de-intercalation was also investigated by using Mn K-edge EXAFS analysis. The Fourier transformed Mn K-edge EXAFS spectra for the SPN7O spinel, before and after lithium de-intercalation, are shown in Fig. 10(a). The first and second FT peaks corresponding to the (Mn–O) and (Mn–Mn) bonding pairs are isolated by inverse Fourier transformation into k space. The resulting $k^3\chi(k)$ Fourier filtered EXAFS oscillations are presented in Fig. 10(b), together with the best fits. The fitted structural parameters are summarized in Table 5. As can be seen in Fig. 10(b), there is a good agreement between the experimental and calculated data, even for the charged sample. This suggests that the spinel lattice is maintained before and after lithium de-intercalation. The fitting results demonstrate that the (Mn–O) bond distance decreases markedly upon de-intercalation of lithium, and therefore, the manganese ion is oxidized. The observed structural change induced by the charging process is considered to be one of the reasons for capacity loss during cycling.

Table 5
Results of non-linear, least-square curve fitting for the first and second shells of Mn K-edge EXAFS spectra for the $LiMn_2O_4$ spinels, SPN4O, SPN5O, SPN6O, SPN7O, and charged SPN7O

Sample	Bond	CN[a]	ΔE (eV)	R (Å)	σ^2 ($10^{-3} \times$ Å)
SPN4O	(Mn–O)	5.07	−4.38	1.885	3.53
	(Mn–Mn)	5.07	−4.40	2.890	3.79
SPN5O	(Mn–O)	5.57	−1.78	1.897	4.22
	(Mn–Mn)	5.57	−4.20	2.889	4.63
SPN6O	(Mn–O)	5.96	−1.90	1.897	4.33
	(Mn–Mn)	5.96	−4.58	2.887	4.74
SPN7O	(Mn–O)	6	0.53	1.908	5.88
	(Mn–Mn)	6	−1.98	2.902	4.91
charged	(Mn–O)	5.67	−2.63	1.896	5.08
SPN7O	(Mn–Mn)	5.67	−6.74	2.870	5.92

[a] In order to check out the evolution of coordination number (CN) upon lowering of the sintering temperature and the charging process, all the CN values are determined by using the amplitude reduction factor (S_0^2) of SPN7O.

4. Conclusions

In this study, a modified citrate route with an ethanol dehydration of Li–Mn–citrate complex solution is established as an effective method for preparing nanocrystalline $LiMn_2O_4$ particles. The present citrate-derived spinel oxides exhibit better electrochemical performance for lithium extraction (4-V) domain, compared with the lithium manganate prepared by a solid-state reaction. Systematic studies of the relationship between the physicochemical properties of $LiMn_2O_4$ and the sintering temperature/atmosphere show that oxygen annealing depresses the cycleability of high-temperature samples due to a broad distribution of particle size, whereas it improves the electrochemical performance of low-temperature samples by reducing inorganic and organic impurities. On the other hand, the XANES/EXAFS analyses for $LiMn_2O_4$ nanoparticles before and after the charging process provide direct evidence of shortening of the (Mn–O) and (Mn–Mn) bond distances upon Li de-intercalation, indicating an increase in Mn oxidation. It is suggested that a marked change in crystal

structure with charging is responsible for the capacity fading.

Acknowledgements

This work was supported in part by the Institute of Information Technology and Assessment (IITA). The synchrotron radiation experiments at PLS were supported in part by MOST and POSCO. The authors are also grateful to Dr. S.H. Chang and Dr. S.G. Kang of ETRI for assisting with the electrochemical measurements.

References

[1] T. Ohzuku, M. Kitogawa, T. Hirai, J. Electrochem. Soc. 137 (1990) 769.
[2] J.M. Tarascon, E. Wang, F.K. Shakoohi, W.R. Mckinnon, S. Colson, J. Electrochem. Soc. 138 (1991) 2859.
[3] M.M. Thackeray, Prog. Solid St. Chem. 25 (1997) 1.
[4] A.F. Wells, Structural Inorganic Chemistry, Clarendon Press, Oxford, 1984, p. 577.
[5] M.M. Thackeray, P.J. Johnson, L.A. Picciotto, P.G. Bruce, J.B. Goodenough, Mater. Res. Bull. 19 (1984) 179.
[6] W.I.F. David, M.M. Thackeray, L.A. Picciotto, J.B. Goodenough, J. Solid State Chem. 67 (1987) 316.
[7] A. Mosbach, A. Verbaere, M. Tournoux, Mater. Res. Bull. 18 (1983) 1375.
[8] P. Barboux, J.M. Tarascon, F.K. Shokoohi, J. Solid State Chem. 94 (1991) 185.
[9] L. Guohua, H. Ikuta, T. Uchida, M. Wakihara, J. Electrochem. Soc. 143 (1996) 178.
[10] J.M. Tarascon, W.R. McKinnon, F. Coowar, T.N. Bowmer, G. Amatucci, D. Guyomard, J. Electrochem. Soc. 141 (1994) 1421.
[11] T. Tsumura, A. Shimizu, M. Inagaki, Solid State Ionics 90 (1996) 197.
[12] Y. Xia, M. Yoshio, J. Power Sources 57 (1995) 125.
[13] Z. Jiang, K.M. Abraham, J. Electrochem. Soc. 143 (1996) 1591.
[14] H. Huang, P.G. Bruce, J. Electrochem. Soc. 141 (1994) L106.
[15] W. Liu, G.C. Farrington, F. Chaput, B. Dunn, J. Electrochem. Soc. 143 (1996) 1591.
[16] S. Bach, M. Henry, N. Baffier, Livage, J. Solid State Chem. 88 (1990) 325.
[17] T. Tsumura, S. Kishi, H. Konno, A. Shimizu, M. Inagaki, Thermochim. Acta 278 (1996) 135.
[18] D. Hennings, W. Mayr, J. Solid State Chem. 26 (1978) 329.
[19] J.H. Choy, Y.S. Han, J.T. Kim, Y.H. Kim, J. Mater. Chem. 5 (1995) 57.
[20] V.K. Sankaranarayanan, Q.A. Pankhurst, D.P.E. Dickson, C. Johnson, J. Magn. Magn. Mater. 120 (1993) 73.
[21] E. Zhecheva, R. Stoyanova, M. Gorava, R. Alcantara, J. Moralez, J.R. Tirado, Chem. Mater. 8 (1996) 1429.
[22] S.R.S. Prabaharan, M.S. Michael, T.P. Kumar, A. Mani, K. Athinarayanaswamy, R. Gangadharan, J. Mater. Chem. 5 (1995) 1035.
[23] H. Yasushi, Nippondenso, U.S. Patent 5565688, 1996.
[24] A. Frenkel, E.A. Stern, A. Voronel, M. Qian, M. Newville, Phys. Rev. B 49 (1994) 11662.
[25] P.A. O'Day, J.J. Rehr, S.I. Zabinsky, G.E. Brown Jr., J. Am. Chem. Soc. 116 (1994) 2938.
[26] F.M.M. Morel, Principles of Aquatic Chemistry, Wiley, New York, 1983.
[27] C.F. Baes Jr., R.E. Mesmer, The Hydrolysis of Cations, Wiley, New York, 1976.
[28] J.H. Choy, Y.S. Han, J. Mater. Chem. 7 (1997) 1815.
[29] B.D. Cullity, Elements of X-ray Diffraction, Addison-Wesley, MA, 1978, p. 284.
[30] S.J. Gregg, K.S.W. Sing, Adsorption, Surface Area and Porosity, Academic Press, New York, 1982, p. 26.
[31] R.J. Gummow, A. Kock, M.M. Thackeray, Solid State Ionics 69 (1994) 59.
[32] P. Endres, B. Fuchs, S. Kemmler-Sack, K. Brandt, G. Faust-Becker, H.W. Praas, Solid State Ionics 89 (1996) 221.